Title: Increased snowfall over the Antarctic Ice Sheet mitigated 20th century sea level rise

Authors: B. Medley[1†] and E.R. Thomas[2]

Affiliations:

[1]NASA Goddard Space Flight Center, Cryospheric Sciences Laboratory, Greenbelt, MD 20771, USA.

[2]British Antarctic Survey, Cambridge, UK CB3 0ET.

[†]Correspondence to: brooke.c.medley@nasa.gov.

Changes in accumulated snowfall over the Antarctic Ice Sheet (AIS) have an immediate and time-delayed impact on global mean sea level (GMSL). The former is due to the instantaneous change in freshwater storage over the ice sheet; the latter acts in delayed opposition through enhanced ice-dynamic flux into the ocean[1]. Here, we reconstruct 200 years of Antarctic-wide snow accumulation by synthesizing a newly compiled database of ice-core records[2] using reanalysis-derived spatial coherence patterns. Results reveal that increased snow accumulation mitigated 20^{th} century sea-level rise by ~10 mm since 1901, with rates increasing from 1.1 mm dec^{-1} between 1901 and 2000 to 2.5 mm dec^{-1} after 1979. Reconstructed accumulation trends are highly variable in both sign and magnitude at the regional scale, linked to the trend toward a positive Southern Annular Mode (SAM) since 1957[3]. Because the observed SAM trend is accompanied by a decrease in AIS accumulation, changes in the strength and location of the circumpolar westerlies cannot explain the reconstructed increase, which may instead by related to stratospheric ozone depletion[4]. Our results indicate that a warming atmosphere, however, cannot be excluded as a dominant force in the underlying increase.

Annual accumulated snowfall over the grounded Antarctic Ice Sheet amounts to ~6 mm of global sea-level equivalence; thus, both short- and long-term variations have a significant and direct impact on sea-level change. GMSL is currently rising[5], but the overall contribution from the AIS remains poorly constrained[6]. Advances in satellite technology have vastly improved our understanding of ice-dynamic thinning and acceleration, around the periphery of the ice sheet[6, 7], yet the potential for ice-sheet-wide observations of snow accumulation fluctuations remains equivocal, designating mass input as arguably the largest source of uncertainty in AIS mass balance estimates. Modeling efforts have significantly reduced this knowledge gap[8], yet without any advancements in AIS accumulation observations, distinguishing between the varying ability of and assigning realistic uncertainties to the modeled net precipitation fields is not possible.

Atmospheric models suggest that snowfall over the AIS will likely rise as atmospheric warming increases its moisture-holding capacity[8]. Significant warming trends[9, 10] over much of the Antarctica Peninsula (AP) and West Antarctic Ice Sheet (WAIS) hint at the possibility of enhanced snowfall, when considering thermodynamical changes alone. Surprisingly, investigation into this potential sea-level mitigation has received little attention, which we surmise stems from (i) the paucity of observed changes at appropriate spatiotemporal scales[11] and (ii) the fact that observation-based atmospheric reanalyses are not trustworthy prior to the satellite era[12]. The publication of research[11] indicating no substantial change in AIS snow accumulation between 1957 and 2005 nearly contemporaneously with a study[9] that found significant warming over much of the AIS, except portions of the East Antarctic Ice Sheet (EAIS), suggests that the relationship between temperature and accumulation is more complex and strongly supports the need for further study into recent AIS accumulation variability and its role in the AIS contribution to GMSL.

Ice core records of snow accumulation (SA), the combination of precipitation, sublimation/evaporation and deposition, wind redistribution, and meltwater runoff, provide enough temporal context (several decades to centuries) for trend evaluation, yet they fall short of sampling the entire AIS[2] and are noisy due to small-scale variability (e.g., sastrugi)[13]. We use 'snow accumulation' over 'surface mass balance' because we are restricted to areas where the latter is positive, which is the case for nearly the entire grounded AIS[14]. Atmospheric reanalyses provide spatiotemporally complete precipitation-minus-evaporation ($P-E$) products that are nearly equivalent to SA over the dry, grounded AIS, and are most trustworthy over the satellite era (1979–present). Notable biases in reanalysis $P-E$ exist[15, 16], however, they reproduce a significant portion of the interannual variability[17]. Here, we modify the methodology in ref.[11] to reconstruct 19th and 20th century SA over the entire grounded AIS and surrounding islands using a combination of ice core records and atmospheric reanalysis $P-E$. A long-term, observationally based reconstruction of SA is necessary to (i) ensure that any significant trends are observable over the noise, (ii) quantify the role of AIS SA on observed sea-level change, (iii) better quantify the relative importance of thermodynamical versus dynamical precipitation change, and (iv) provide an AIS-wide observation-based SA record, along with uncertainties, for robust evaluation of global and regional atmospheric AIS net precipitation estimates.

Combining 53 ice core records with the spatial patterns of $P-E$ from three reanalyses, we reconstruct the 1801-2000 annual SA over the grounded AIS and surrounding islands (Fig. 1a; Supplementary Table S1 and Supplementary Figs. S1-S2). We only show results from reconstruction based on MERRA-2 $P-E$ fields: R_{MERRA2}. The R_{MERRA2} performed better than the ERA-Interim- and CFSR-based reconstructions (R_{ERAI} and R_{CFSR}) because: (i) the reanalysis showed the least bias in total magnitude (Supplementary Fig. S3) and (ii) exhibited the highest skill in reproducing the observations (see Supplementary Methods; Supplementary Fig. S4 and Supplementary Table S2). Here, we refer to the performance of the reconstruction and not the reanalysis product itself. In addition, we find that the reconstructions replicate a significant portion of the reanalysis $P-E$ variability between 1980 and 2000 even though a few of the ice cores used do not (Supplementary Fig. S5).

Trends in SA over the 20th century (1901−2000) and late 20th century (1957−2000) indicate that inhomogeneous patterns of change dominate any AIS-wide signal (Fig. 1a-c), and that mass is being significantly redistributed regionally over the AIS since the 1957–58 International

Geophysical Year (IGY) and likely since the onset of the 20th century. Integrated over the entire ice sheet, however, we observe a clear and significant positive trend in SA (Fig. 2a). A steady increase is found over the EAIS, although it has reversed in the late 20th century (Fig. 2b) even though local trends strengthened in the latter half (Fig. 1b). We also observe a strong see-saw pattern of increased SA over the AP and eastern WAIS contrasted with decreased accumulation over the western WAIS. After nearly a century of decreasing SA over the AP, we find a rapid and potentially accelerating increase over the 20th century (Fig. 2d), whereas the gains and losses from western and eastern WAIS largely balance (Fig. 2c). Because the reconstruction is spatiotemporally complete, we determine the net SA contribution to GMSL over the 20th century by integrating the annual accumulation relative to the 19th century mean (1801–1900; Fig. 2) through time.

Between 1901 and 2000, SA over the AIS and its peripheral islands mitigated GMSL by 1.12 ± 0.45 mm dec^{-1}; however, that rate has more than doubled to 2.47 ± 0.76 mm dec^{-1} after 1979 (Fig. 3a). We determine that only the EAIS (0.77 ± 0.40 mm dec^{-1}) and WAIS (0.28 ± 0.17 mm dec^{-1}) mitigated GMSL over the 20th century, but recent SA increases over the AP suggest that it will enter the 21st century as a source of significant GMSL mitigation (0.62 ± 0.17 mm dec^{-1}). Decreasing EAIS SA since 1979 indicates a potential slowdown in mitigation from this sector, while the opposite is true for the AP. It is critical to note that these sea-level mitigation values are based only on mass input to the AIS and do not account for the observed increases in mass output from glaciers that are in dynamic imbalance such as Pine Island and Thwaites[6, 18].

AIS-wide SA significantly mitigated 20th century GMSL, but did it result from thermodynamical or dynamical precipitation change? The Southern Annular Mode (SAM), defined by a belt of low pressure surrounding the Antarctic that controls the strength and position of the circumpolar westerlies, is the dominant mode of atmospheric variability in the high-latitude Southern Hemisphere[19]. Since the 1957–58 IGY, the annual SAM index has exhibited a strong positive trend[3] largely due to anthropogenic ozone depletion and increased atmospheric greenhouse-gas concentrations[20], leading to a contraction of the belt of westerlies towards the Antarctic continent[21]. The pattern and magnitude of SAM-congruent trends and reconstructed SA trends are remarkably similar (Fig. 1c–d), which indicates that changes in atmospheric circulation are a dominant force. Of note, we performed additional reconstructions after first removing the SAM-congruent $P-E$ signal from each reanalysis, and the results are nearly identical; thus, the pattern is independent and robust (see Supplementary Methods; Supplementary Figs. S6-S7). Our reconstructions indicate that the positive SAM trend explains ~80% ($n > 20{,}000$ and $p << 0.001$) of the spatial variability in the 1957–2000 trends, suggesting anthropogenically driven atmospheric circulation changes are largely responsible for the snow mass redistribution over the AIS.

These findings are complicated by the simple fact that a *positive* trend in SAM phase is accompanied by a *negative* trend in AIS-wide net precipitation in all three reanalyses. Thus, if an evolving SAM was solely responsible for the temporal trends in our reconstruction since 1957, we would expect that AIS-wide SA would *contribute* to SLR rather than *mitigate*. In fact, the SAM-congruent SA trend reduced the 1957–2000 GMSL mitigation by more than 2.5 mm.

Thus, we investigate the likelihood that the observed SA increases are due to atmospheric warming over the AIS. Investigation of the trend residuals (Fig. 1e) suggests that there are underlying positive SA trends over much of the AIS, especially coastal EAIS and most of WAIS and the AP (Supplementary Table S5). Because the positive trends are spatially pervasive, they are likely not attributable to changes in large-scale atmospheric circulation, which imparts a unique snowfall signature of often counteracting trends based on the relationship between wind anomalies and the regional topography[22]. Despite uncertainties in the reconstruction, as well as the SAM trend, the atmospheric warming required to account for the residual trends are consistent with modelling and observational efforts[9, 10, 23] (Table 1). Specifically, moderate temperature trends of 0.27, 0.17, and 0.06 °C dec^{-1} are needed over the AP, WAIS, and the EAIS, respectively. Strengthening or weakening of the positive trend in the SAM index shifts the warming between the AP and WAIS, and thus, their combined warming remains nearly unchanged. Approximately 40% ($n > 20{,}000$ and $p \ll 0.001$) of the spatial variability in the residual trends can be explained by the $P-E$ sensitivity to temperature, indicating that the regions most sensitive to temperature change are experiencing the largest changes. Thus, we cannot eliminate a warming atmosphere as the driver of the underlying SA increases.

A prior reconstruction found an insignificant negative trend in AIS-wide SA, suggesting that accumulation was not mitigating ice losses around the periphery and that atmospheric circulation variability, not thermodynamic moisture change, is the dominant driver[11]. We argue that our results are not incompatible with their findings. From a temporal standpoint, we find a positive, statistically insignificant trend (1.0 ± 1.3 Gt yr^{-2}) between 1957 and 2000; however, when the peripheral islands are included, the trend narrowly emerges as significant (1.4 ± 1.4 Gt yr^{-2}). Furthermore, our reconstruction is based solely on the ice-core time series, whereas ref.[11] used ERA-40 $P-E$ from 1985–2005, which is the source of the negative trend. We use only observation-based values due to observing system artifacts in the reanalysis $P-E$ that compromise trend analysis[15]. Additionally, we find that circulation-driven precipitation change does impart a large signal on AIS-wide trends that are spatially heterogeneous, masking any underlying increases. Finally, we observe significant and insignificant decreasing trends over the

EAIS (-4.5 ± 3.5 Gt yr^{-2}) and AIS (-2.7 ± 3.8 Gt yr^{-2}) since 1979, respectively, matching the trend sign in the prior reconstruction[11]. Thus, the differences of methodology combined with the strength of the SAM-congruent snowfall signature suggest that our results are not inconsistent with ref.[11].

While the temporal change in SA imparts a clear trend on GMSL mitigation, the spatial patterns of trend magnitude and sign have potential glaciological implications. Present-day rates of ice discharge across the grounding zone likely contain an atmospherically-driven component that varies in scale and direction depending on its location[1]. We demonstrate that ice mass is being significantly redistributed across the AIS, highlighting the need for improved understanding of expected atmospherically-driven ice dynamical changes to isolate regions of change that exceed this surface climate signal.

Evaluation of our 200-year reconstruction of AIS-wide SA suggests that climate-change-related dynamical and potentially thermodynamical forces likely control the observed spatiotemporal trends with the former outweighing the latter since 1957, masking the underlying positive SA trends. We cannot eliminate atmospheric warming as the source of SA GMSL mitigation, especially considering the temperature trends necessary to account for the residual SA trends are similar to temperature reconstructions. Recent work[4] suggests that increased SA since the mid-20th century might be attributable to stratospheric ozone depletion. A mechanistic link was not uncovered, however, exposing the complexity of the relationship between ozone depletion, the strength and location of the circumpolar westerlies, air temperature, and ultimately accumulation.

Modern-day accumulation over the AIS is 78.6 ± 26.5 Gt yr^{-1} higher than the 19th century mean, a value more than 1.5 times the AIS rate of mass loss during the 1990s[24]. Nevertheless, net AIS mass loss[24] (2720 ± 1390 Gt) over just 26 years (1992–2017) has accounted for 70% of the century long SA gains (3815 ± 1105 Gt). An insignificant negative trend in AIS SA hints at the possibility of a reduction in annual mass gain after 2000; however, even if frozen at 78.6 Gt yr^{-1}, SA gains are a mere 1/3rd of the AIS mass losses (219 ± 43 Gt yr^{-1}) indicating that SA is not keeping pace with oceanic-driven ice mass loss.

Fig. 1 | Trends in reconstructed Antarctic-wide snow accumulation and their relationship to the Southern Annular Mode. Absolute accumulation trends over 1901–2000 **(a)**, 1901–1956 **(b)**, and 1957–2000 **(c)** with regions significance at the 1-sigma confidence level enclosed by the dashed lines. The grey open circles show ice core locations. The 1957–2000 SAM-congruent $P-E$ trend **(d)** is removed from the reconstructed trend **(c)**, revealing the residual trend **(e)** that is not explained by the dominant mode of atmospheric variability in the high-latitude Southern Hemisphere.

Fig. 2 | Nineteenth and twentieth century relative annual accumulation by Antarctic sector. Net accumulation over the (a) Antarctic Ice Sheet, (b) East Antarctic Ice Sheet, (c) West Antarctic Ice Sheet, and (d) Antarctic Peninsula, relative to the 19th century mean (dashed line). The shaded bounds are the 1-sigma uncertainties. The solid and dashed colored lines represent significant and insignificant trends over various intervals, and the slope (*m*) and intercept (*b*) are included in a table above each time series (see Trend Analysis in Methods).

Fig. 3 | Twentieth century cumulative mass and sea-level change due to snow accumulation. **(a)** The R_{MERRA2} cumulative mass (left axis) and equivalent sea-level change (right axis) by Antarctic sector over the 20th century, relative to the 19^{th} century mean. The dashed lines represent a time-integrated model of mass change based on the linear regression statistics presented in Fig. 2. For clarity, the error bounds are included for the AIS only, and their derivation is described in Methods: Sea-level mitigation. **(b)** Mass and sea-level mitigation by 2000 for each of the three reconstructions where the vertical lines show error bounds. The horizontal bar and shaded area represent the mean and combined uncertainty of all three reconstructions. All error bounds represent the $\pm 1\sigma$ range.

Methods

Snow accumulation over the grounded AIS and its surrounding islands are reconstructed on the premise that the variability at a specific location has an associated spatial signature (i.e., regions that have a direct and indirect coherence). While distance is likely a factor here, we must recognize the complex interaction of topography and predominant wind direction in generating orographic effects not controlled by distance alone. Therefore, we use modeled spatial signatures from atmospheric reanalysis $P-E$ as the basis of our interpolation weighting scheme. Because of their aforementioned skill in reproducing the interannual variability[17], which largely controls the skill of the weighting scheme, we use global atmospheric reanalyses over regional climate models.

The reconstruction method applied here is an improvement upon a prior study[11] that provides sufficient detail to replicate the work; thus, we only briefly describe the methodology and describe our modifications. Rather than rely on a single reanalysis model, we generate three reconstructions based on different atmospheric reanalyses including ERA-Interim, MERRA-2, and CFSR (see below), whereas ref.[11] relied only on ERA-40. In such a manner, we created three reconstructions, where each used the same ice-core observations but different modeled spatial weights, giving no preference to a specific model. The reanalyses have different observing and assimilation systems and spatial grids; therefore, it is only reasonable to expect site-specific spatial signatures to vary to some extent.

Our validation analysis of the reconstructions is very thorough and is thus detailed in the Supplementary Methods section. All references within the methods refer to the validation within the Supplementary Methods section along with several Supplementary Tables and Figures.

Global atmospheric models

We created annual $P-E$ products from three global atmospheric reanalysis products, specifically the European Centre for Medium-Range Weather Forecasts "Interim" (ERA-Interim)[25], the NASA Modern Era Retrospective Analysis for Research and Applications version 2 (MERRA-2)[26], and the National Centers for Environmental Prediction Climate Forecast System Reanalysis (CFSR)[27]. We specifically use ERA-Interim monthly means of twice-daily 12-hour forecast accumulations of total precipitation and evaporation, MERRA-2 monthly mean total precipitation and evaporation, and CFSR monthly mean of 6-hour forecast accumulations of total precipitation and 6-hour averages of latent heat flux, which are converted to sublimation using the latent heat of sublimation (2,838 kJ kg^{-1}).

The CFSR data are the combination of two versions of CFSR: version 1 spans 1979–2010 and version 2 spans 2011–2016. We repeated the reconstruction using only version 1 data, but the results did not vary significantly. To keep consistency with the ERA-Interim and MERRA-2 reanalyses, we use the combined CFSR record (1979–2016).

The modeled spatial signatures are based on the full reanalysis time period (1979–2016: ERA-Interim, CFSR; 1980–2016: MERRA-2) using $P-E$ time series normalized to the overlapping period with the all ice core records (1980–1988). The latter ensures all measurements are relative to the same interval while the former provides as long of a climatological context as possible for the reconstruction. Similar to ref.[11], we generate spatial weights for each ice core by calculating its shared variance with all locations via the coefficient of determination (r^2).

Ice core data

We use 53 annually resolved ice core records of snow accumulation, the majority of which are available in a newly compiled database[2], that cover a substantial portion of the AIS and a few surrounding islands (Supplementary Fig. S1). Of the 80 records in the database, we use 52 for the reconstruction (Supplementary Table S1). We require that each record spans the 1980-1988 period to provide several years of overlap with the reanalyses and to maximize the number of cores used in the reconstruction (Supplementary Fig. S2). We also exclude several records that do not exhibit fully annual resolution throughout the entire record, which come largely from the early site survey for the European Project for Ice Core Drilling in Dronning Maud Land (EPICA-DML). One newly published record is added to the data set: the B40 record[28]. The maximum correlation at each grid point with the reanalysis-based $P-E$ at each ice core site indicates the ice core coverage is very good, especially over West Antarctica and the Antarctic Peninsula (Supplementary Fig. S8). Weaker correlations over the high plateau suggest we would benefit from additional observations from these locations. However, accumulation rates are so low over the East Antarctic plateau that it is extremely challenging to create an annually resolved record.

Unlike ref.[11], we opt to include all records whether they span the full reconstruction interval (1801–2000) or not. Only 16 records span the entire interval, and coverage is not sufficient to fully capture the accumulation variability especially over the EAIS and AP (Supplementary Fig. S8). Under our premise, the minimum number of records used is 29 for any year (Supplementary Fig. S2). Based on the distribution of records that exist at the beginning (1801) and end (2000) of our reconstruction interval, we capture the common variability (Supplementary Fig. S8).

To assess our ability to reconstruct the variability, we perform an additional reconstruction using the $P-E$ values directly from the reanalysis in a “best-case” scenario. For each year of the reconstruction, we use the reanalysis $P-E$ records for the given ice-core combination and attempt to reconstruct the entire reanalysis $P-E$ field. In such a manner, we can assess the proportion of variability explained at each grid cell under each ice-core combination, providing insight into our ability to capture AIS-wide accumulation variability. Supplementary Table S3 contains the accumulation-weighted expected proportion of variance explained over the entire record and over the different sectors. The results indicate that we are typically able to explain about 61% of the variance in AIS snow accumulation over the entire 200-year interval; however, that proportion dips only somewhat to 59% and 51% for 1801 and 2000, respectively. Thus, we conclude that even with gaps in our ice-core network, we are consistently able to capture a large portion of the variability in AIS-wide snowfall.

To ensure that we are not introducing spurious artifacts in our reconstructed trends, we also perform a cross-validation reconstruction using only the 16 complete records, and is termed the *ComplCore* reconstruction. We find that the trends in the full and *ComplCore* reconstructions are similar, which is explained in more detail in the validation section below.

Reanalysis P−E bias

The atmospheric reanalysis $P-E$ products exhibit biases in total magnitude across much of the AIS that vary substantially from one another[15]. Using observations of annual surface mass balance from the ice core data presented above, radar-derived measurements over the Pine Island and Thwaites glacier catchments[18], and an AIS-wide database[29] of surface mass balance, we assess the magnitude bias in the three reanalyses used in our study (Supplementary Fig. S3). Although it limited our spatial coverage, we only used observations from ref.[29] that fell within (and only within) the reanalysis period (1979/80–2016). The surface mass balance values were then compared to the modeled $P-E$ from the grid cell to which they belong for the contemporaneous years, $bias = (model - observation) / model$. If multiple observations exist for a single grid cell, they are averaged together to create one bias correction per cell. In such a manner, we found the relative error in the modeled $P-E$ magnitudes that were then interpolated over the entire AIS using the statistical interpolation method of kriging (i.e., distance-based interpolation).

Bias correction can potentially influence our results since change is calculated relative to the mean annual accumulation. Thus, if the bias correction is incorrect (or incomplete), the quality of the estimated sea-level impact is compromised. To assess whether to use the bias corrected reconstructions, we compare the validation statistics from the bias and non-bias-corrected reconstructions for R_{MERRA2}, R_{ERAI}, and R_{CFSR}. The final reconstructions are bias-corrected for R_{MERRA2} and R_{ERAI} and non-bias-corrected for R_{CFSR} because those reconstruction scenarios outperformed the other. Mitigation values by the year 2000 are very similar between the final reconstructions (R_{MERRA2}: 10.6 mm, R_{ERAI}: 11.0 mm, R_{CFSR}: 9.7 mm), suggesting that the reconstructed trends are similar even though the actual magnitudes are different. We determine that R_{MERRA2} is the most robust since it exhibits the least bias in magnitude (Supplementary Fig. S3) and as a result, sea-level mitigation from the bias- and non-bias-corrected R_{MERRA2} are 10.6 mm and 10.8 mm, respectively, and are essentially identical.

Reconstruction Error Analysis

We generate gridded annual uncertainty for the reconstructed accumulation rates by accounting for both measurement error (i.e., small scale variability or noise in the ice core records) and the uncertainty introduced by the spatial sampling of cores. While modeled $P–E$ is often biased over the AIS, it can reproduce the interannual variability with some skill[17]. At the same time, trends in reanalysis products are sometimes untrustworthy as shifts in the observing system can generate spurious jumps through time[15]. Therefore, we assess the noise (or uncertainty) in each ice-core record by calculating the root mean square error (RMSE) between the detrended record and the reanalysis time series at the grid cell corresponding to the location of the ice core. We assign the final uncertainty for each record, as the minimum of the standard deviation of the reanalysis time series and RMSE. These values comprise the observational uncertainty in units of normalized accumulation and are propagated through on a cell-by-cell and year-by-year basis.

Accounting for the uncertainty introduced from limited spatial sampling is extremely important. A reconstruction based on two ice-core records will have a much larger uncertainty than one based on 10s of records and that uncertainty will vary in space. To determine the uncertainty due to the sampling geometry of the cores, we perform the reconstruction a second time replacing the ice core time series with the reanalysis time series from each of the ice core sites. Essentially, we assess our ability to recreate the reanalysis $P-E$ records over the entire AIS by using only a subset of reanalysis time series that correspond to the locations of the ice core records. This uncertainty will vary with time as the number of cores used in the reconstruction varies in time. Specifically, we determine the spatiotemporal RMSE of this reanalysis-based reconstruction by comparing it with the actual reanalysis data. These values comprise the sampling errors in units of normalized accumulation. The final uncertainty product is the square root of the sum of squares of the two sources of uncertainty (observation and sampling errors).

Spatial Integration

To determine mass change on a cell-by-cell basis, we scale the grid cell SA (mm w.e. yr^{-1}) by the area of the grounded ice within the grid cell. The basins are defined by ref.[30] and the sectors are defined as follows: the EAIS basins are 2-17 (10.1×10^6 km^2), WAIS are 1 and 18-23 (1.8×10^6 km^2), the AP are 24-27 (0.2×10^6 km^2). The entire AIS (12.2×10^6 km^2) and surrounding islands (0.2×10^6 km^2) are defined by the MODIS mosaic of Antarctica grounded ice and islands vector data sets[31], and their combination represents the total area of grounded ice in the Antarctic (12.4×10^6 km^2).

To generate the sector time series, we combine the mass time series over the entire area of each spatial region of interest. The associated uncertainty time series accounts for the spatial correlation of grid cell time series (i.e., highly correlated, dependent records yield higher uncertainties than if all the records were entirely independent of one another): rather than taking the square of the sum of the square errors, we scale the uncertainties by the correlation (or dependence) of each pair of records. In such a manner, we account for the fact that many of the cells within a spatial region of interest are based primarily on the same core records, reducing their independence and thus increasing their uncertainties.

Trend Analysis

To determine the trends in SA and their associated uncertainties, we use a Monte Carlo method to generate n = 10,000 simulations of the 1801–2000 sector-integrated time series of SA (Fig. 2) by adding random noise to the original time series that is normally distributed with a mean of zero and standard deviation equal to the propagated uncertainty. We then calculate the trend of each realization with time zeroed at the middle of the time interval of interest, providing an intercept approximately equal to the mean of the time series over that interval. Our final trends and intercepts (Fig. 2) and their respective errors are the mean and standard deviation of all the realizations. The intercept (Gt yr^{-1}) represents the mean annual relative SA over the period of interest, and if positive and significant, indicates that sector is mitigating sea-level rise over that time interval. The slope (Gt yr^{-2}) is an indicator of whether mitigation from a given sector is undergoing an acceleration. These regression statistics represent a simple model of SA behavior, and when integrated, provide the modeled sea-level mitigation curves in Fig. 3.

Sea-level mitigation

To evaluate the role of AIS SA on 20th century sea-level change, we assume that 19th century mass input via SA is representative of the long-term mean for an AIS in balance. This choice is justified by the fact that out of the 28 records that extend beyond the 19th century, 23 records have 19th century mean annual accumulation rates equal to the mean over the entire record based on a two-sample two-tailed Student's t test with 95% confidence ($300 \leq df \leq 2155$). Therefore, 19th century accumulation is likely a tenable substitute for a longer-term (several century) mean in the absence of sufficient observations. Cumulative mass change is determined by accumulating the relative annual SA (Fig. 2) with time, which is then converted to sea-level equivalence by dividing by 361 Gt.

To determine the rates of sea-level mitigation and their uncertainties, we use a Monte Carlo method to generate n = 10,000 simulations of the 1801–2000 sector-integrated time series of SA (Fig. 2) by adding random noise to the original time series that is normally distributed with a mean of zero and standard deviation equal to the propagated uncertainty. Next, we determine the cumulative mass change of each realization, where the uncertainty (shaded area in Fig. 3) is the standard deviation of the simulated cumulative mass time series. Such a method allows us to capture the impact of uncertainty in the 19th century mean annual SA rather than relying solely on the regression statistics from 1901 onward presented in Fig. 2.

SAM-congruent trends

We estimate the SAM-congruent trends in SA by first assessing the $P-E$ sensitivity to deviations in the SAM. After calculating the reanalysis-based SAM index[32], we perform cell-by-cell linear regression between the detrended $P-E$ and SAM timeseries. Unfortunately, the reanalyses begin in 1979/80, so in order to get a longer-term perspective on the role of an evolving SAM, we use a proxy-based SAM index[3] that extends back to 1957. The $P-E$ sensitivity to the SAM is next multiplied by the 1957–2000 SAM index trend (0.59 ± 0.20 dec^{-1}), providing the SAM-congruent trend in $P-E$ (Fig. 1d). To evaluate residuals, we remove the SAM-congruent trend signal from our reconstruction (Fig. 1e). The patterns and magnitudes are robust across all three reanalysis reconstructions (Supplementary Fig. S10) as well as the *RemoveSAM* cross-validation reconstructions.

***P−E* sensitivity to air temperature**

We assess $P-E$ sensitivity to the 2-meter air temperature through linear regression of their detrended timeseries on a cell-by-cell basis, providing the change in $P-E$ for every degree change in temperature. While these models show spurious trends and shifts in temperature[15], we are purely exploiting the relationship between temperature and accumulation. We find that the three models have similar sensitivities over the AIS (ERA-Interim: 192 Gt °C^{-1}, MERRA-2: 233 Gt °C^{-1}, CFSR: 264 Gt °C^{-1}) with MERRA-2 falling in the middle, which is potentially because ERA-Interim and CFSR $P-E$ values are biased low and high, respectively. We next divide the residual trends in Fig. 1e by the $P-E$ sensitivity to temperature to estimate the temperature trend required to explain reconstructed trends that are not attributable to the SAM. We present the area-weighted mean associated temperature trends over each sector in Table 1. To account for uncertainty in the trend in the SAM index, we perform the same exercise using the upper (SAM High) and lower (SAM Low) 1-sigma trend bounds.

Code availability

The code for generating the reconstructions is available at the NASA Goddard Cryosphere data portal (https://neptune.gsfc.nasa.gov/csb/).

Data availability

The snow accumulation reconstructions generated and analyzed during this study are available at the NASA Goddard Cryosphere data portal (https://neptune.gsfc.nasa.gov/csb/). The reanalysis data are available as follows: CFSR (https://rda.ucar.edu/pub/cfsr.html), ERA-Interim (https://www.ecmwf.int/en/forecasts/datasets/archive-datasets/reanalysis-datasets/era-interim) , and MERRA-2 (https://disc.gsfc.nasa.gov/). The ice core records are hosted at https://ramadda.data.bas.ac.uk/repository/entry/show?entryid=83f2ca40-04b5-4029-a04c-c18b202dc2f8.

Acknowledgements

We would like to acknowledge all involved in collection and analysis of the ice core records used in our reconstruction, and manuscript comments from A. Barker and J. Lenaerts. B.M. and E.R.T. were respectively supported by NASA's ICESat-2 Project Science Office and the British Antarctic Survey (Natural Environment Research Council). Finally, we thank three anonymous referees for their constructive comments, which vastly improved the quality of the work.

Author Contributions

All authors designed the study. B.M. wrote the manuscript with input from E.R.T. E.R.T. analyzed the ice-core records, and B.M. performed the reconstruction and its analysis thereafter.

Competing Interests

The authors declare no competing interests

References

1. Winkelmann, R., Levermann, A., Martin, M. A. & Frieler, K. Increased future ice discharge from Antarctica owing to higher snowfall. *Nature* **492**, 239 (2012).

2. Thomas, E. R. *et al*. Review of regional Antarctic snow accumulation over the past 1000 years. *Climate of the Past Discussions* **2017**, 1-42 (2017).

3. Marshall, G. J. Trends in the Southern Annular Mode from observations and reanalyses. *J. Clim.* **16**, 4134-4143 (2003).

4. Lenaerts, J. T. M., Fyke, J. & Medley, B. The Signature of Ozone Depletion in Recent Antarctic Precipitation Change: A Study With the Community Earth System Model. *GRL* **45** (2018).

5. Beckley, B. *et al*. Assessment of the Jason-2 extension to the TOPEX/Poseidon, Jason-1 sea-surface height time series for global mean sea level monitoring. *Mar. Geod.* **33**, 447-471 (2010).

6. Shepherd, A. *et al*. A Reconciled Estimate of Ice-Sheet Mass Balance. *Science* **338**, 1183-1189 (2012).

7. Pritchard, H. D., Arthern, R. J., Vaughan, D. G. & Edwards, L. A. Extensive dynamic thinning on the margins of the Greenland and Antarctic ice sheets. *Nature* **461**, 971-975 (2009).

8. Palerme, C. *et al*. Evaluation of current and projected Antarctic precipitation in CMIP5 models. *Clim. Dyn.* **48**, 225-239 (2017).

9. Steig, E. J. *et al*. Warming of the Antarctic ice-sheet surface since the 1957 International Geophysical Year. *Nature* **457**, 459-462 (2009).

10. Nicolas, J. P. & Bromwich, D. H. New reconstruction of Antarctic near-surface temperatures: Multidecadal trends and reliability of global reanalyses. *J. Clim.* **27**, 8070-8093 (2014).

11. Monaghan, A. J. *et al*. Insignificant Change in Antarctic Snowfall Since the International Geophysical Year. *Science* **313**, 827-831 (2006).

12. Schneider, D. P. & Fogt, R. L. Artifacts in century□length atmospheric and coupled reanalyses over Antarctica due to historical data availability. *Geophys. Res. Lett.* (2018).

13. McConnell, J. R., Mosley□Thompson, E., Bromwich, D. H., Bales, R. C. & Kyne, J. D. Interannual variations of snow accumulation on the Greenland Ice Sheet (1985–1996): New observations versus model predictions. *Journal of Geophysical Research: Atmospheres* **105**, 4039-4046 (2000).

14. van Wessem, J. M. *et al*. Modelling the climate and surface mass balance of polar ice sheets using RACMO2: Part 2: Antarctica (1979-2016). *Cryosphere* **12**, 1479-1498 (2018).

15. Bromwich, D. H., Nicolas, J. P. & Monaghan, A. J. An Assessment of Precipitation Changes over Antarctica and the Southern Ocean since 1989 in Contemporary Global Reanalyses. *J. Climate* **24**, 4189-4209 (2011).

16. Palerme, C. *et al*. Evaluation of Antarctic snowfall in global meteorological reanalyses. *Atmos. Res.* **190**, 104-112 (2017).

17. Medley, B. *et al*. Airborne-radar and ice-core observations of annual snow accumulation over Thwaites Glacier, West Antarctica confirm the spatiotemporal variability of global and regional atmospheric models. *Geophys. Res. Lett.* **40**, 3649-3654 (2013).

18. Medley, B. *et al*. Constraining the recent mass balance of Pine Island and Thwaites glaciers, West Antarctica, with airborne observations of snow accumulation. *The Cryosphere* **8**, 1375-1392 (2014).

19. Thompson, D. W. & Wallace, J. M. Annular modes in the extratropical circulation. Part I: month-to-month variability*. *J. Clim.* **13**, 1000-1016 (2000).

20. Arblaster, J. M. & Meehl, G. A. Contributions of external forcings to southern annular mode trends. *J. Clim.* **19**, 2896-2905 (2006).

21. Van Den Broeke, Michiel R & Van Lipzig, N. P. Changes in Antarctic temperature, wind and precipitation in response to the Antarctic Oscillation. *Annals of Glaciology* **39**, 119-126 (2004).

22. Fyke, J., Lenaerts, J. T. & Wang, H. Basin-scale heterogeneity in Antarctic precipitation and its impact on surface mass variability. *The Cryosphere* **11**, 2595 (2017).

23. Stenni, B. *et al*. Antarctic climate variability on regional and continental scales over the last 2000 years. *Climate of the Past* **13**, 1609 (2017).

24. Shepherd, A. *et al*. Mass balance of the Antarctic Ice Sheet from 1992 to 2017. *Nature* **556**, pages219–222 (2018).

Methods References

25. Dee, D. P. *et al*. The ERA-Interim reanalysis: configuration and performance of the data assimilation system. *Q. J. R. Meteorol. Soc.* **137**, 553-597 (2011).

26. Gelaro, R. *et al*. The Modern-Era Retrospective Analysis for Research and Applications, Version 2 (MERRA-2). *J. Climate* **30**, 5419-5454 (2017).

27. Saha, S. *et al*. The NCEP Climate Forecast System Reanalysis. *Bull. Amer. Meteor. Soc.* **91**, 1015-1057 (2010).

28. Medley, B. *et al*. Temperature and snowfall in western Queen Maud Land increasing faster than climate model projections. *Geophys. Res. Lett.* **45**, 1472-1480 (2018).

29. Favier, V. *et al*. An updated and quality controlled surface mass balance dataset for Antarctica. *The Cryosphere* **7**, 583-597 (2013).

30. Zwally, H. J., Giovinetto, M. B., Beckley, M. A. & Saba, J. L. Antarctic and Greenland Drainage Systems. *GSFC Cryospheric Sciences Laboratory* (2012).

31. Bohlander, J. & Scambos, T. Antarctic coastlines and grounding line derived from MODIS Mosaic of Antarctica (MOA), Boulder, Colorado USA: National Snow and Ice Data Center. *Digital media* (2007).

32. Gong, D. & Wang, S. Definition of Antarctic oscillation index. *Geophys. Res. Lett.* **26**, 459-462 (1999).

Table 1. Temperature trends required to account for residual trends in reconstructed SA based on $R_{MERRA-2}$. The snow accumulation sensitivity to near-surface air temperature is provided. Mean temperature trends are the area-weighted mean over each sector, and the lower and upper quartile bounds by area are in parentheses. Temperature trends from four reconstructions over a similar time interval from ref.[10] and reconstructed 20th century trends from ref.[23] are shown.

	SA Sensitivity to Temperature (Gt °C^{-1})	Mean Temperature Trend (lower - upper quartile; °C dec^{-1})			1960 - 2005 Temperature Trends (°C dec^{-1})[10]				20th Century Temperature Trends[23] (°C dec^{-1})
		SAM	SAM Low	SAM High	NB14	M10	S09	O11	
AIS	233.3	0.08 (-0.01 - 0.16)	0.04 (-0.06 - 0.13)	0.11 (0.01 - 0.19)					0.04 ± 0.03 - 0.10 ± 0.09
EAIS	146.4	0.06 (-0.03 - 0.13)	0.02 (-0.07 - 0.11)	0.09 (0.01 - 0.16)	0.04 ± 0.12	0.10 ± 0.16	0.11 ± 0.12	0.05 ± 0.11	0.01 ± 0.12 - 0.04 ± 0.03
WAIS	64.9	0.17 (0.09 - 0.23)	0.12 (0.02 - 0.20)	0.20 (0.11 - 0.32)	0.19 ± 0.15	0.20 ± 0.16	0.16 ± 0.10	0.08 ± 0.09	0.06 ± 0.06 - 0.13 ± 0.09
AP	22.4	0.27 (0.07 - 0.35)	0.34 (0.16 - 0.44)	0.18 (-0.02 - 0.29)	0.29 ± 0.19	0.39 ± 0.22	0.11 ± 0.07	0.30 ± 0.13	0.11 ± 0.06 - 0.29 ± 0.11
Islands	11.6	0.15 (0.01 - 0.28)	0.20 (0.02 - 0.37)	0.10 (-0.05 - 0.22)					
AIS + Islands	245.0	0.08 (-0.01 - 0.16)	0.05 (-0.05 - 0.14)	0.11 (0.01 - 0.19)					
WAIS + AP	87.3	0.18 (0.09 - 0.23)	0.15 (0.03 - 0.22)	0.20 (0.09 - 0.32)					

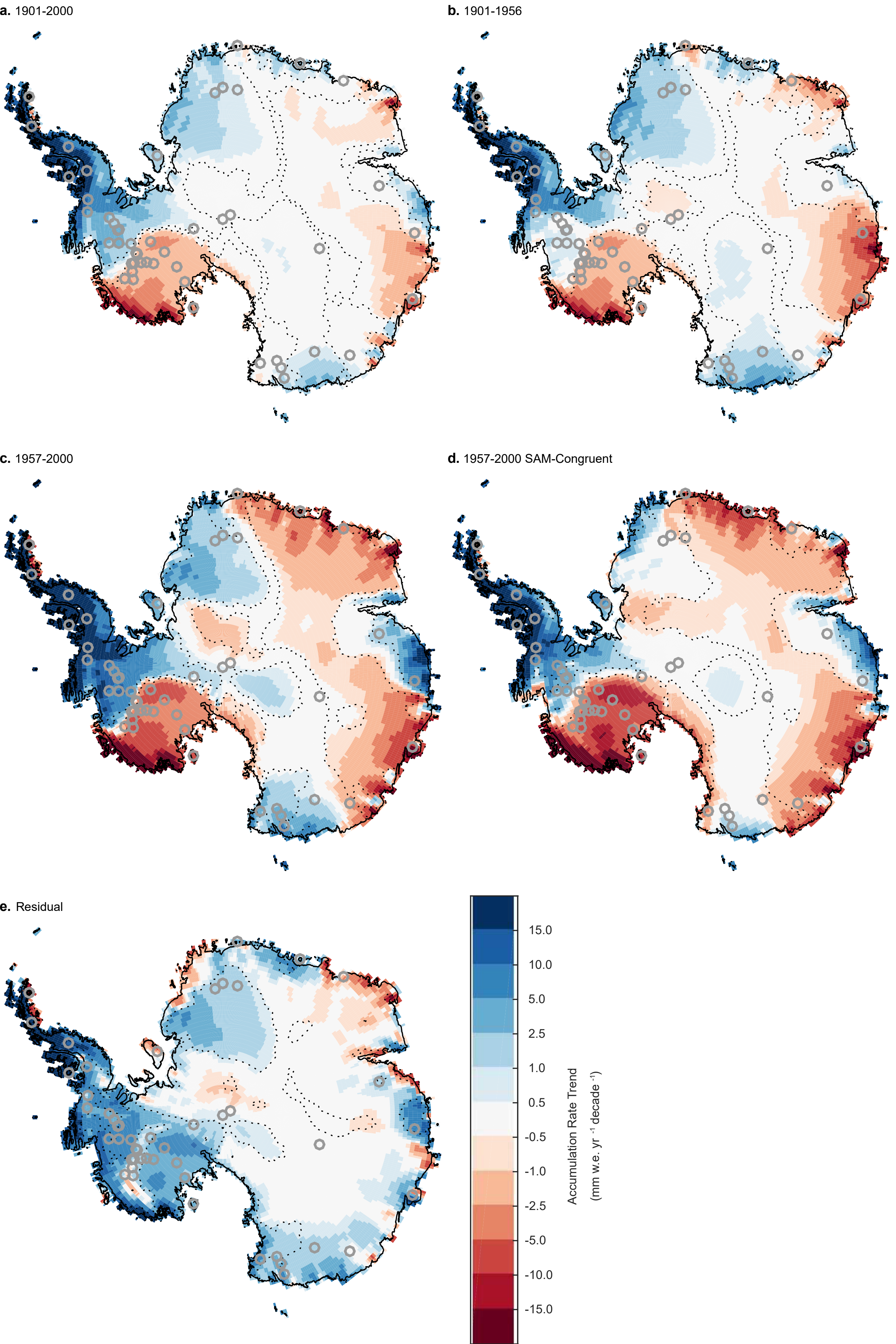
a. 1901-2000
b. 1901-1956
c. 1957-2000
d. 1957-2000 SAM-Congruent
e. Residual
15.0
10.0
5.0
2.5
1.0
0.5
-0.5
-1.0
-2.5
-5.0
-10.0
-15.0
Accumulation Rate Trend
(mm w.e. yr -1 decade -1)

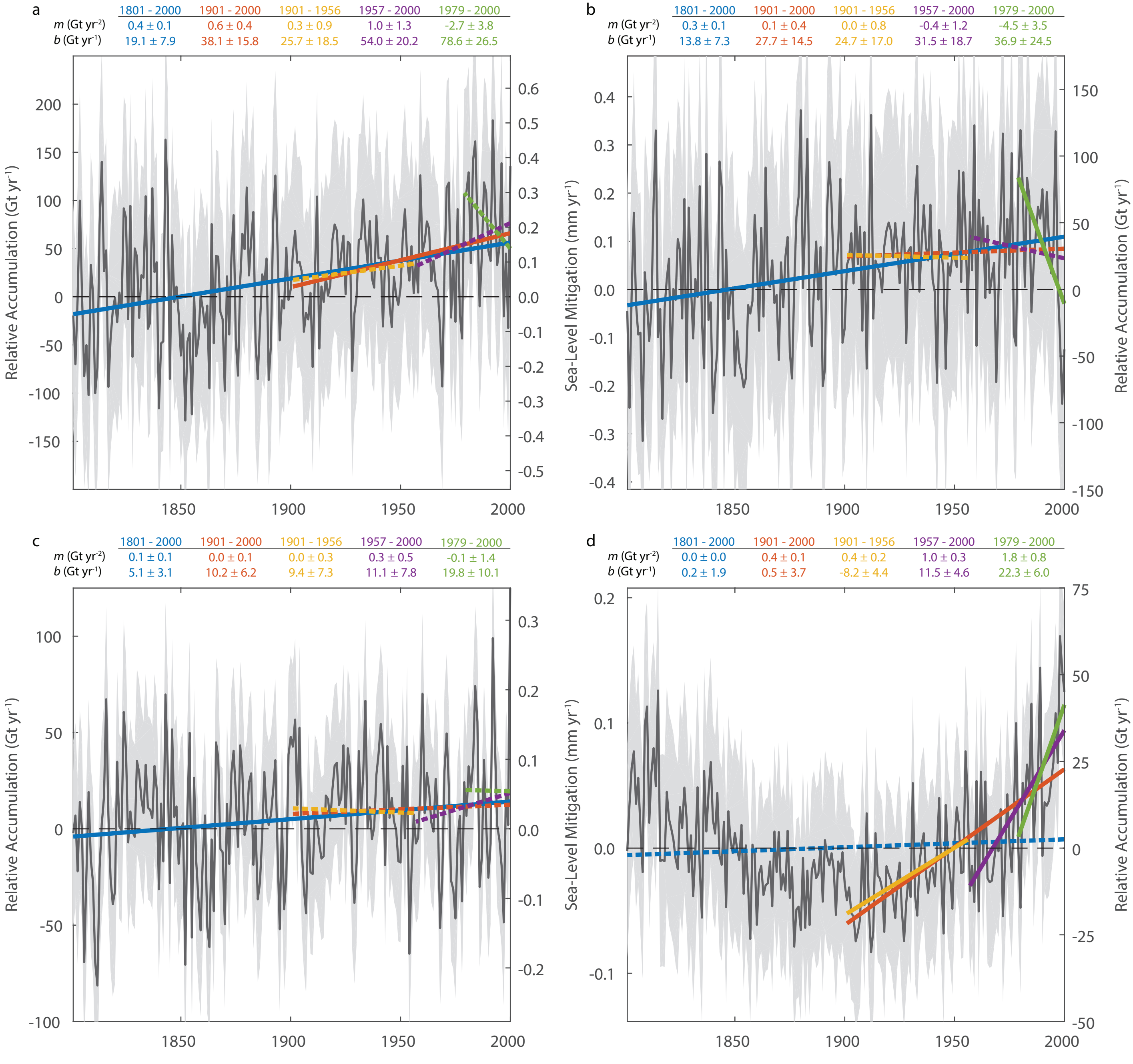
a
1801 - 2000 | 1901 - 2000 | 1901 - 1956 | 1957 - 2000 | 1979 - 2000
m (Gt yr-2) 0.4 ± 0.1 | 0.6 ± 0.4 | 0.3 ± 0.9 | 1.0 ± 1.3 | -2.7 ± 3.8
b (Gt yr-1) 19.1 ± 7.9 | 38.1 ± 15.8 | 25.7 ± 18.5 | 54.0 ± 20.2 | 78.6 ± 26.5
Relative Accumulation (Gt yr-1)
b
1801 - 2000 | 1901 - 2000 | 1901 - 1956 | 1957 - 2000 | 1979 - 2000
m (Gt yr-2) 0.3 ± 0.1 | 0.1 ± 0.4 | 0.0 ± 0.8 | -0.4 ± 1.2 | -4.5 ± 3.5
b (Gt yr-1) 13.8 ± 7.3 | 27.7 ± 14.5 | 24.7 ± 17.0 | 31.5 ± 18.7 | 36.9 ± 24.5
Sea-Level Mitigation (mm yr-1)
Relative Accumulation (Gt yr-1)
c
1801 - 2000 | 1901 - 2000 | 1901 - 1956 | 1957 - 2000 | 1979 - 2000
m (Gt yr-2) 0.1 ± 0.1 | 0.0 ± 0.1 | 0.0 ± 0.3 | 0.3 ± 0.5 | -0.1 ± 1.4
b (Gt yr-1) 5.1 ± 3.1 | 10.2 ± 6.2 | 9.4 ± 7.3 | 11.1 ± 7.8 | 19.8 ± 10.1
Relative Accumulation (Gt yr-1)
d
1801 - 2000 | 1901 - 2000 | 1901 - 1956 | 1957 - 2000 | 1979 - 2000
m (Gt yr-2) 0.0 ± 0.0 | 0.4 ± 0.1 | 0.4 ± 0.2 | 1.0 ± 0.3 | 1.8 ± 0.8
b (Gt yr-1) 0.2 ± 1.9 | 0.5 ± 3.7 | -8.2 ± 4.4 | 11.5 ± 4.6 | 22.3 ± 6.0
Sea-Level Mitigation (mm yr-1)
Relative Accumulation (Gt yr-1)
1850
1900
1950
2000

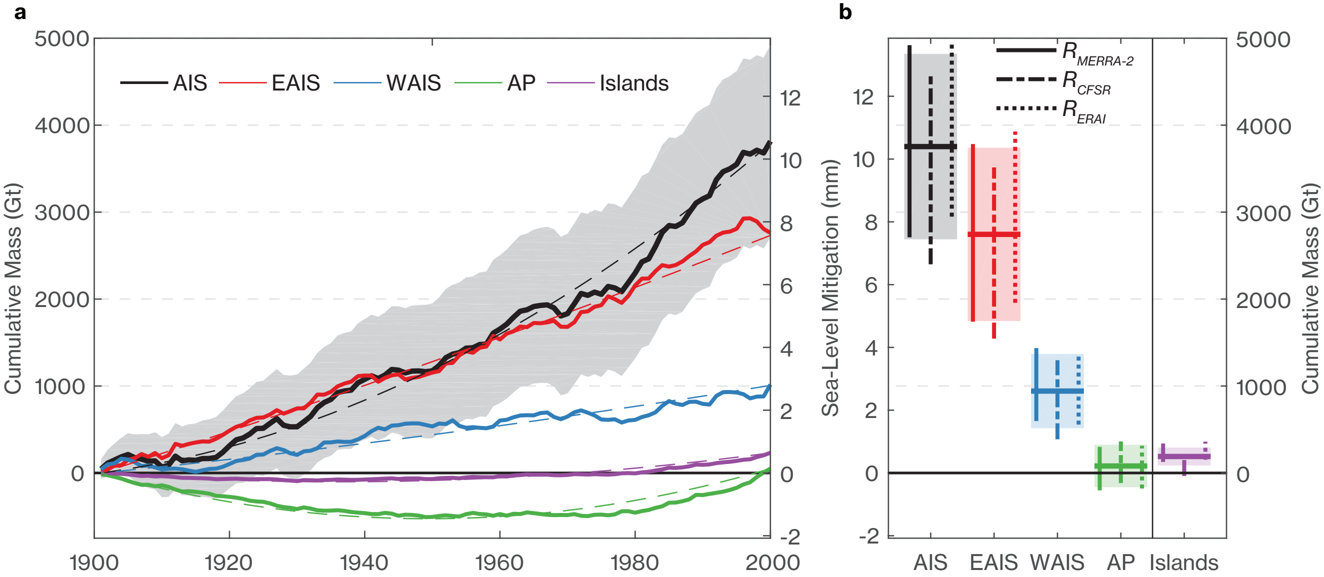
a
b
AIS
EAIS
WAIS
AP
Islands
Cumulative Mass (Gt)
5000
4000
3000
2000
1000
0
1900
1920
1940
1960
1980
2000
12
10
8
6
4
2
0
-2
Sea-Level Mitigation (mm)
R MERRA-2
R CFSR
R ERAI
AIS
EAIS
WAIS
AP
Islands